Violent expiratory events: on coughing and sneezing

Citation: Bourouiba, Lydia, Eline Dehandschoewercker, and John W. M. Bush. "Violent Expiratory Events: On Coughing and Sneezing." Journal of Fluid Mechanics 745 (March 24, 2014): 537–563.

As Published: http://dx.doi.org/10.1017/jfm.2014.88

Publisher: Cambridge University Press

Persistent URL: http://hdl.handle.net/1721.1/101386

Version: Final published version: final published article, as it appeared in a journal, conference proceedings, or other formally published context

J. Fluid Mech. (2014), *vol.* 745, *pp.* 537–563.
doi:10.1017/jfm.2014.88

Violent expiratory events: on coughing and sneezing

Lydia Bourouiba[1,2,†], **Eline Dehandschoewercker**[3] **and John W. M. Bush**[1]

[1]Department of Mathematics, Massachusetts Institute of Technology, Cambridge, MA 02130, USA

[2]Department of Civil and Environmental Engineering, Massachusetts Institute of Technology, Cambridge, MA 02130, USA

[3]PMMH - ESPCI, O207 10, rue Vauquelin, 75005 Paris, France

(Received 4 January 2013; revised 29 December 2013; accepted 7 February 2014)

Violent respiratory events such as coughs and sneezes play a key role in transferring respiratory diseases between infectious and susceptible individuals. We present the results of a combined experimental and theoretical investigation of the fluid dynamics of such violent expiratory events. Direct observation of sneezing and coughing events reveals that such flows are multiphase turbulent buoyant clouds with suspended droplets of various sizes. Our observations guide the development of an accompanying theoretical model of pathogen-bearing droplets interacting with a turbulent buoyant momentum puff. We develop in turn discrete and continuous models of droplet fallout from the cloud in order to predict the range of pathogens. According to the discrete fallout model droplets remain suspended in the cloud until their settling speed matches that of the decelerating cloud. A continuous fallout model is developed by adapting models of sedimentation from turbulent fluids. The predictions of our theoretical models are tested against data gathered from a series of analogue experiments in which a particle-laden cloud is ejected into a relatively dense ambient. Our study highlights the importance of the multiphase nature of respiratory clouds, specifically the suspension of the smallest drops by circulation within the cloud, in extending the range of respiratory pathogens.

Key words: biological fluid dynamics, multiphase and particle-laden flows, turbulent flows

1. Introduction

Emerging or reemerging viral and bacterial infectious diseases (e.g. H1N1, H5N1, SARS, tuberculosis) have increasingly high human and economic consequences (IMF/World Bank 2006). Confined environments, such as airplanes, hospitals and schools, serve as mixers where pathogens can stay suspended and spread from host to host. Hence, understanding the dynamics of pathogens indoors is critical to improving the modelling and control of epidemics (Settles 2006; Tang *et al.* 2006; Weber & Stilianakis 2008). Nevertheless, the transmission mechanisms of even the most common respiratory diseases remain poorly understood. Three modes of transmission are discussed in the medical literature. *Self-inoculation* may arise through

† Email address for correspondence: lbouro@mit.edu

direct contact with the mucus (or other bodily fluids) of an infectious subject. *Large droplet transmission* may arise through the spraying of infected droplets directly onto the conjunctiva or mucus of a susceptible host via coughing or sneezing. *Airborne transmission* may arise through inhalation of relatively small infected droplets or the pathogen-bearing solid residues of size <5–10 μm, referred to as *droplet nuclei*, that can form from the small droplets via evaporation (e.g. Nicas, Nazaroff, & Hubbard 2005; Tellier 2006). The first two modes are termed *direct* short-range routes of pathogen transmission, both requiring the close proximity of individuals, while the third is an *indirect* long-range route of transmission.

The literature remains undecided as to the relative importance of long-range airborne transmission and short-range large droplet transmission for many diseases, including SARS, avian influenza and whooping cough. For example, Tellier (2006, 2009) and Clark & de Calcina-Goff (2009) vigorously argue the importance of airborne transmission for avian influenza viruses. For SARS, *a posteriori* studies revealed that the transmission involved a combination of two modes, short-range large droplet transmission via direct contact and airborne transmission via transport of droplet nuclei in the ventilation system of healthcare facilities (e.g. Wong *et al.* 2004; Yu *et al.* 2004). The basic mechanisms of direct and indirect pathogen transfer between people remain poorly understood (e.g. Tang *et al.* 2006; Weber & Stilianakis 2008; Bourouiba & Bush 2012). Experimental studies have been aimed at measuring the size distribution of droplets emitted by various respiratory functions, such as coughing and sneezing (e.g. Wells 1934, 1955; Duguid 1945; Loudon & Roberts 1967; Papineni & Rosenthal 1997; Yang *et al.* 2007; Morawska *et al.* 2009*b*; Johnson *et al.* 2011). The discrepancy between reported data on droplet size spectra poses a basic impediment to the mathematical modelling of respiratory disease transmission. Fluid dynamics studies of the cloud resulting from violent expirations have been presented by Settles and coworkers (e.g. Settles 2006; Tang, Path & Settles 2008; Tang *et al.* 2009), who combined schlieren optical method and particle image velocimetry in order to reveal the velocity field within the initial phase of a cough cloud (Jonassen, Settles & Tronosky 2006). Although the dynamics of the gas phase were detailed, the droplet dynamics were not given particular attention.

Violent expirations release multiphase turbulent flows that are generally composed of buoyant hot moist air and suspended droplets of various sizes. These droplets contain components such as pathogens and minerals that can form droplet nuclei after evaporation of the drop's liquid phase. At low Reynolds number, the Stokes settling speed $U_S = gd^2/(18\mu)(\rho_d - \rho)$ of a droplet of diameter d and density ρ_d in an ambient gas phase of density ρ is proportional to its surface area which necessarily decreases with time due to evaporation. It remains a common belief that most contamination of new individuals occurs via direct contact with large droplets emitted by an infectious individual. Wells (1934, 1955) challenged this view and was the first to examine the role of airborne transmission of respiratory disease transmission. He compared the time for complete evaporation to the settling time of various droplets ranging in diameter from 1 to 1000 μm. He reported that drops with diameter $d > 100$ μm settle to the ground in less than 1 s, without significant evaporation (Wells 1934). While evaporation rates will in general depend on ambient temperature and humidity, drops with $d < 100$ μm will typically become droplet nuclei before settling (Wells 1955). Droplets with $d < 5$–10 μm rapidly evolve into droplet nuclei with settling speeds less than 3 mm s^{-1}, and so may be readily suspended and advected by the cloud of air emitted by the cougher, or resuspended by any ambient flow as may arise, for example, through air conditioning. Thus, suspended droplet nuclei are expected to be critical elements in long-range airborne transmission.

The size distribution of respiratory droplets has been the subject of an increasing number of studies (e.g. Duguid 1946), with recent focus on the improvement of the precision of measurement of the small submicrometre range (e.g. Morawska 2006; Johnson *et al.* 2011; Zayas *et al.* 2012). An example of droplet size distribution for coughs is shown in figure 17, which indicates a peak drop size of $\sim$15 μm, the associated settling speed being 6.5 mm s^{-1} in ambient air typical of winter indoor conditions. In addition to having potential for long-range transmission, it is generally thought that smaller drops and particles better penetrate the respiratory tract, reaching deeper target tissues within the lungs. Indeed, experiments of inoculation of animals with respiratory pathogens and solid particles (e.g. Sonkin 1951; Wells 1955) suggest that, given the same viral load, inhalation of the atomized solution results in higher infection and death rates than direct intranasal inoculation.

2. Observations

Puffs, jets, thermals and plumes are turbulent bodies of fluid ejected from a localized source either continuously (in the case of plume and jets) or discontinuously (in the case of puffs and thermals). Thermals and plumes are buoyancy driven, while puffs and jets are momentum driven (Scorer 1978; Turner 1979). As they proceed from the source, these flows retain roughly the same shape and their lateral extent increases linearly with distance from the source. This observation of self-similarity led to the entrainment hypothesis (Morton, Taylor & Turner 1956) which allows one to render such turbulent flows analytically tractable by assuming that the details of the velocity fluctuations can be averaged out. According to the entrainment hypothesis, the speed w of the ambient fluid drawn into the cloud is proportional to the average cloud speed U, so the cloud radius r increases linearly with the distance s from the source: $w = \alpha U$ and $r = \alpha s$ (Morton *et al.* 1956) (figure 1*a*). The values of the entrainment coefficient α are observed to be roughly constant although with considerable variability for each type of flow, be it thermal or plume, puff or jet. This turbulent plume theory has proven to be sufficient to capture key features of many geophysical and environmental flows, including the emission of industrial effluent, the emission of volcanic hydrothermal plumes or thermals and the ejections of bubble plumes in lakes (e.g. Scorer 1978; Cardoso & Woods 1993; Gonnermann & Manga 2007; Woods 2010). Here, we adapt such an approach in order to describe the dynamics of violent expiratory events. The fate of the suspended droplets is determined by drawing an analogy with multiphase particle-laden clouds as arises in a variety of geophysical systems such as riverine outflows or industrial waste discharges (e.g. Scorer 1978; Socolofsky, Crounse, & Adams 2002; Bush, Thurber, & Blanchette 2003; Hunt *et al.* 2007).

We here present the results of a combined experimental and theoretical study aimed at elucidating the dynamics of pathogen-bearing droplet dispersion by violent expiratory events. In § 2, we present the results of our visualization of real human coughs and sneezes. An analogue experimental study of multiphase puffs is presented in § 3, and allows us to refine our physical picture of expiratory clouds. The resulting theoretical model is developed in § 4. The application of our theoretical model to clinical data is presented in § 5.

We began by visualizing the dynamics of coughs and sneezes produced by adults. A schematic illustration of the experimental set-up used in our study is presented in figure 2. The head of the subject was positioned in front of a black felt backdrop in order to create a black-field effect. The area was surrounded with lights oriented to

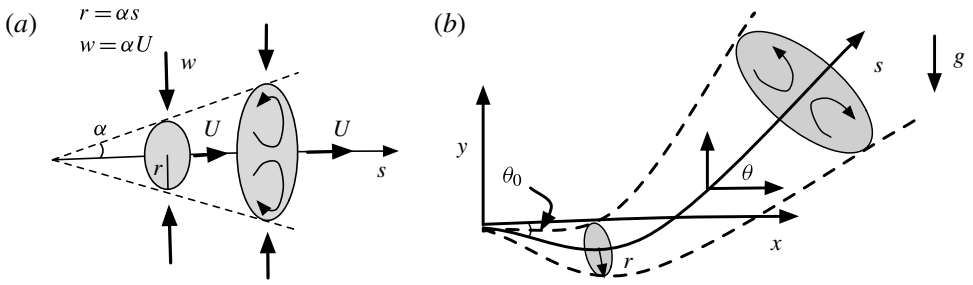

FIGURE 1. (*a*) Schematic of the spreading and settling of the particles from a cloud emitted horizontally. Note the self-similarity of the cloud as it grows by entrainment of the surrounding fluid. (*b*) A schematic illustration of the trajectory of the multiphase buoyant puff of radius $r(t)$ at position $s(t)$ from the source. Gravity deflects the cloud motion from the horizontal, causing it to rise. Note that in this example, the puff is initially shot downward at an angle $\theta_0 \neq 0$.

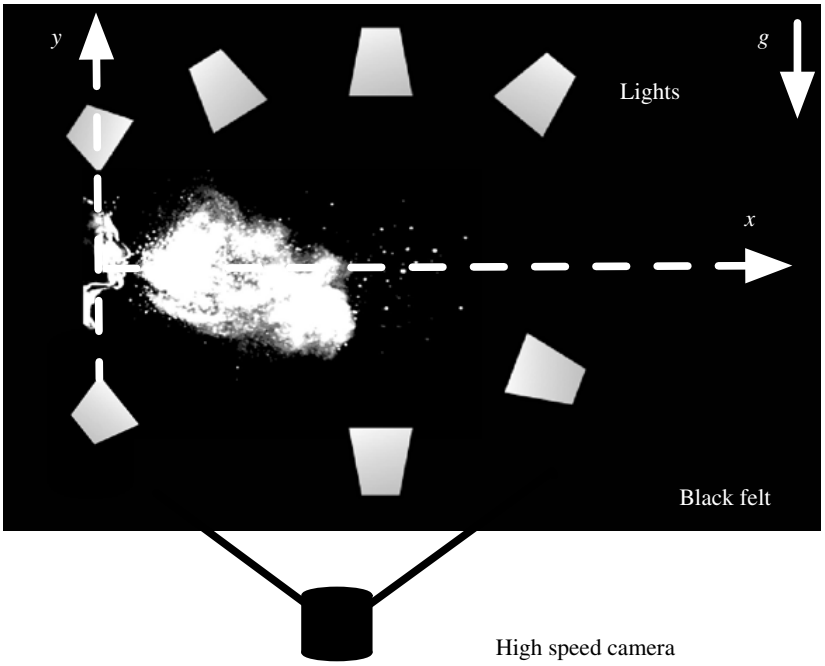

FIGURE 2. Experimental set-up for the visualization of the violent respiratory events using high-speed cameras.

maximize light scattering by the emitted droplets. High-speed imaging of various violent expirations was recorded at 1000–4000 frames per second (f.p.s.) with a Phantom high-speed video. A monochrome camera was used to reduce light sensitivity. Note that despite the high density of ejecta apparent in figures 3 and 4, considerably more droplets and mist were observed with the naked eye than with the camera. Nevertheless, our visualizations were sufficient for our purposes. In certain experiments, a smoke generator enabled tracking of the emitted gas phase. Coughs and sneezes were found to consist of a turbulent cloud of buoyant gas with suspended droplets. The largest droplets follow a ballistic trajectory relatively unaffected by the flow in the gas phase, while the smaller drops were suspended to varying degrees within the turbulent gas cloud, thereby having their range extended.

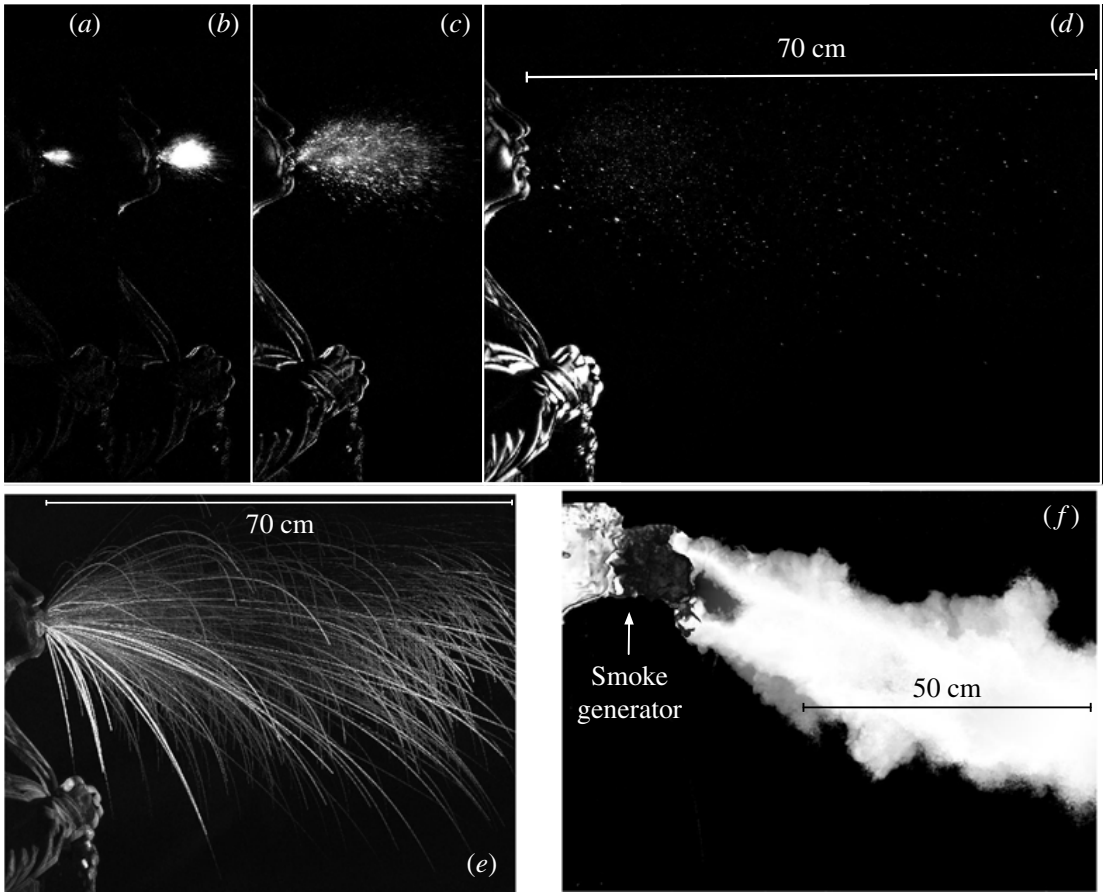

FIGURE 3. High-speed images of a cough recorded at 1000 frames per second (f.p.s.) reveal the dynamics of the expelled gas and liquid phases. The sequence is displayed for the times (*a*) 0.006 s, (*b*) 0.01 s, (*c*) 0.029 s and (*d*) 0.106 s. (*e*) Large droplets are ejected and their trajectories shown in this streak image. (*f*) A typical cough airflow is visualized using a smoke generator and recorded at 2000 f.p.s. Note that (*e*) and (*f*) are the superposition of the instantaneous images of the droplets and cloud trajectories throughout the sequence.

Figure 3(*a–d*) shows the visualization of a cough, recorded at 1000 f.p.s. This sequence shows the time evolution of the emitted spray until 106 ms after the onset of visible droplet emissions. The early images (figure 3*a–c*) indicate the cone-like shape of the ejecta cloud and the high density of droplets emitted by the cougher. The largest droplets are tracked visually, resulting in the streak image shown in figure 3(*e*). The shape of the trajectories suggests a ballistic path for the larger droplets whose dynamics is not greatly affected by the cough cloud. We also used smoke to enhance our visualization of the cough cloud. Figure 3(*e*,*f*) allow us to compare the trajectories of the emitted droplets with the path of the air cloud, as visualized with smoke. The air flow emitted was recorded at 2000 f.p.s. The smoke cloud was initially directed downward at an angle $24 \pm 7^\circ$ from the horizontal and associated with an entrainment coefficient of 0.24 ± 0.02 in the initial jet phase close to the mouth and 0.132 ± 0.06 in the second puff phase. The airflow was expelled for approximately 300 ms as highlighted by the use of smoke in figure 3(*f*), where we superpose the video sequence from the onset of the cough to the end of

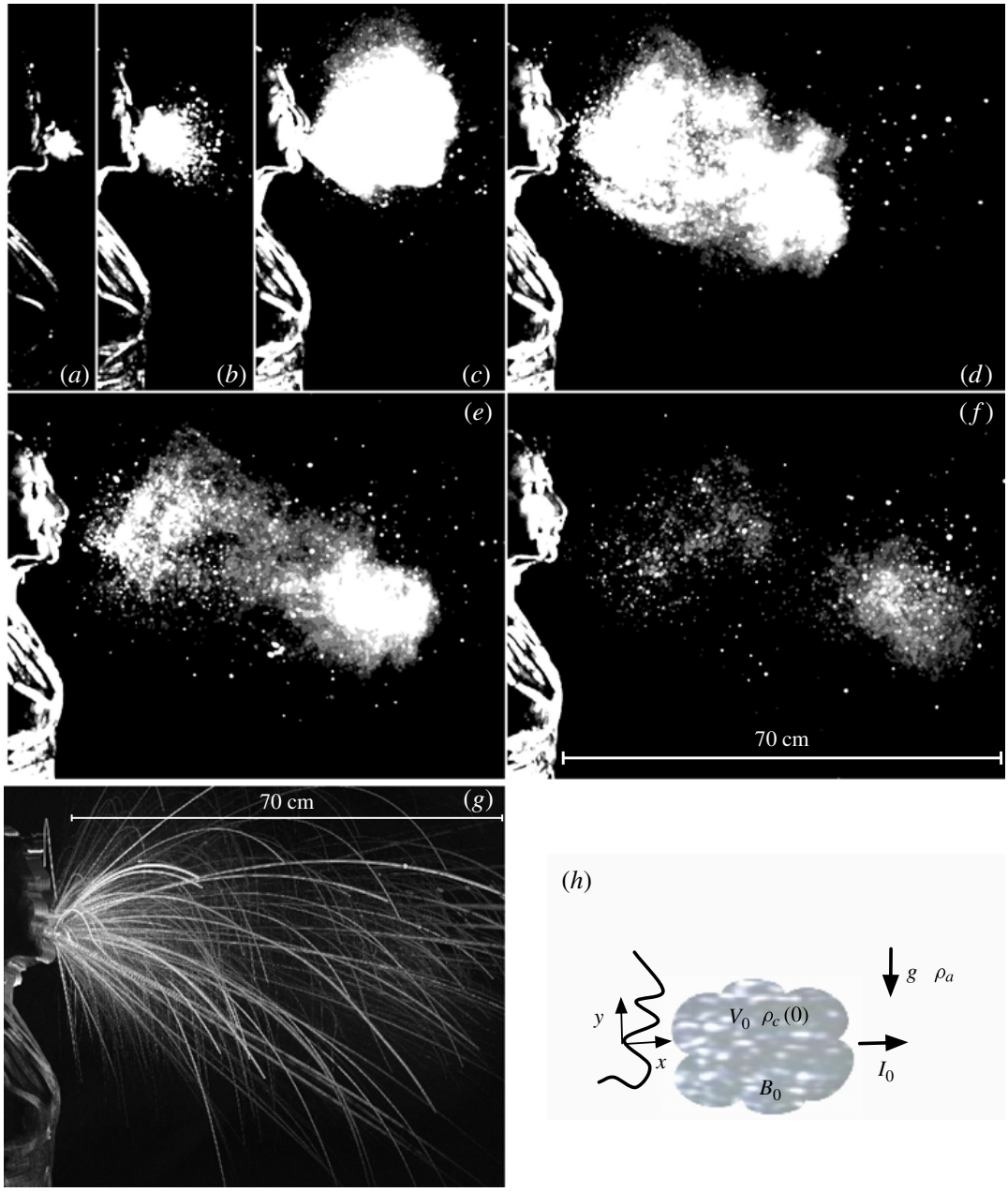

FIGURE 4. (Colour online) High-speed images recorded at 1000 f.p.s. of a sneeze at times (*a*) 0.006 s, (*b*) 0.029 s, (*c*) 0.106 s, (*d*) 0.161 s, (*e*) 0.222 s and (*f*) 0.341 s. (*g*) Trajectories of the largest droplets are revealed through a streak image. (*h*) A schematic of the initial cloud with characteristic initial momentum I_0, buoyancy B_0 and volume V_0 emitted into quiescent ambient air.

the recording. The duration of coughs was estimated to be 200–500 ms in Gupta, Lin & Chen (2009), with peak flows arising at 57–110 ms for female subjects and 57–96 ms for males and opening angle close to the mouth leading to approximate entrainment coefficient of 0.21. Our observations are thus consistent with the ranges previously reported. The expelled volume of the female subject in figure 3(*f*) was estimated to be 0.6 ± 0.1 l by recording the volumes of water displaced by a series

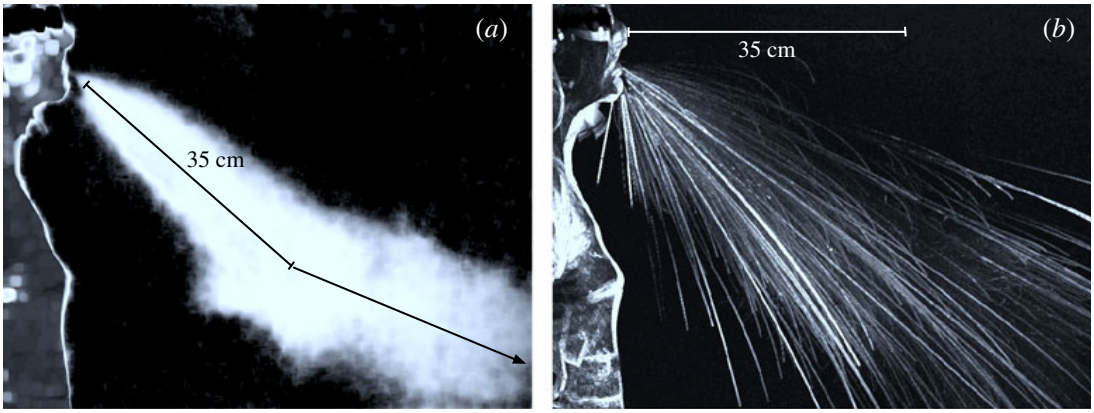

FIGURE 5. (Colour online) (*a*) The effect of buoyancy on the sneeze cloud is apparent in its upward curvature. (*b*) The large droplet trajectories are shown in the streak image recorded at 2000 f.p.s.

of coughs directed into a bath via a tube. By way of comparison, measurements on large groups of patients reported that the volume expired during coughs was in the range 0.25–1.25 l for females and 0.4–1.6 l for males (McCool 2006; Gupta *et al.* 2009; Park *et al.* 2010). The mouth opening area in this figure was estimated to be 3.4 cm^2 during the cough, which is also consistent with values reported in previous studies, 4 ± 0.95 cm^2 for males and 3.37 ± 1.4 cm^2 for females (Gupta *et al.* 2009).

Figure 4 shows analogous visualizations of a sneeze recorded at 1000 f.p.s. The top series of images shows the evolution of the cloud from 0.006 to 0.34 s from the onset of the sneeze. The cloud is evidently more dense than that generated by the cough (figure 3); moreover, the range of visible droplets is larger. Figure 4(*g*) shows the trajectories of the largest droplets emitted in the sneeze, whose dynamics are markedly different from those of the smaller drops transported within the cloud. Sneezes were also observed to be shorter than coughs for the same individual, the observed duration being approximately 200 ms. Our visualizations capture the dynamics of the cloud up to approximately 1 m from the source. Using the observed ejection speed and geometry, we estimate a typical Reynolds number of 10^4 for coughing and 4×10^4 for sneezing. The estimated entrainment coefficients for the sneeze shown in figure 5 are 0.13 ± 0.02 in the initial jet phase and 0.055 ± 0.01 in the subsequent puff phase.

Figure 5 shows the comparison between the trajectory of the exhaled sneeze cloud and the larger droplets recorded at 2000 f.p.s. The cloud trajectory was particularly helpful to visualize the effect of buoyancy. The values of momentum and buoyancy of the cloud vary with distance from the source as ambient air is entrained and the droplets settle out of the cloud. We note that the apparent kink in the trajectory of the cloud, a common feature in the sneezes recorded, occurs at a time where the average momentum and buoyancy of the cloud become comparable, as will be discussed further in section § 4.

Figure 6 shows an image sequence of a sneeze recorded at 2000 f.p.s. The circulation within the cloud is readily apparent on the video and highlighted in this figure with a pair of arrows. Note the change of orientation of the arrows, which again illustrates the influence of buoyancy in deflecting the cloud upward. One can clearly see the trace of the mist droplets that remain suspended and recirculated within the sneeze cloud even beyond 70 cm from the source. The residual mist suspended in the cloud remains apparent until the end of the video. We also observe the settling

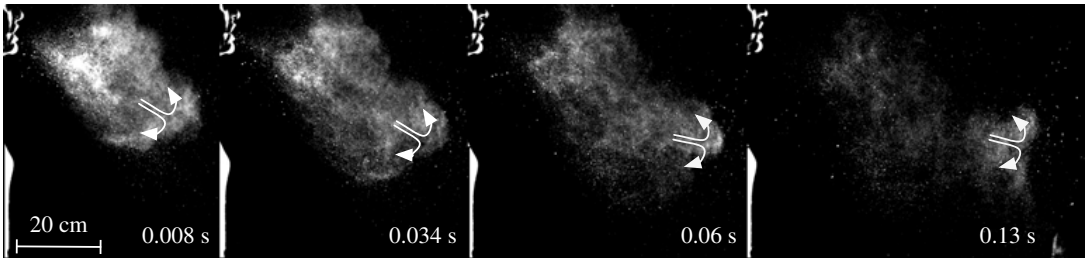

FIGURE 6. An image sequence of a sneeze cloud indicating the interaction between the gas and fluid phases. The arrows illustrate the apparent circulation within the cloud. The change in direction of the cloud is also shown by the shift in the direction of the arrows. The total release time of this sneeze was 200 ms. Time since initial release is indicated in each frame. The smallest mist droplets remain suspended until the end of the video, over 1.35 s.

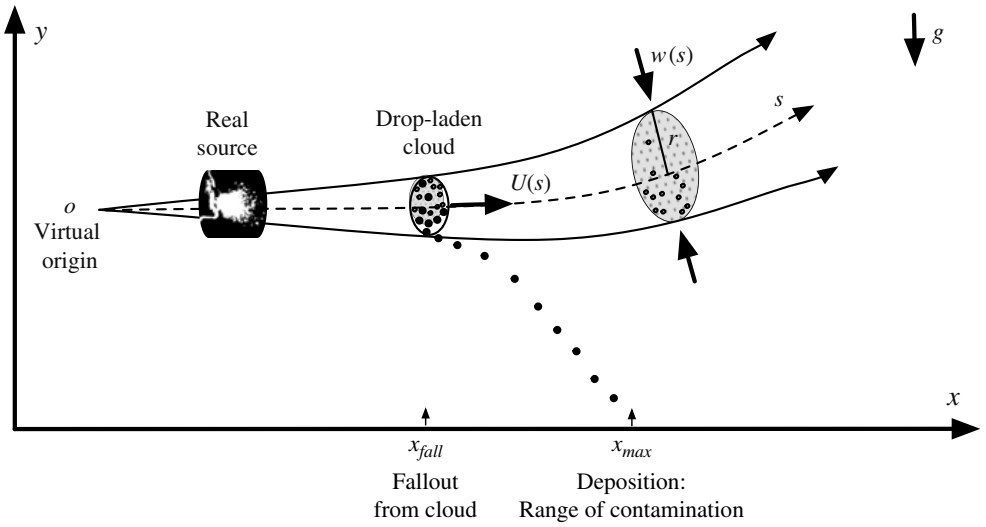

FIGURE 7. Physical picture of the evolution of a cough or sneeze cloud emitted horizontally. Negatively buoyant suspended droplets are circulated within the cloud until they settle out (at a horizontal distance x_{fall}) and reach a final position x_{max}, corresponding to the range of contamination. The virtual origin is shown behind the sneezer source and is computed by extrapolating the measured trajectory of the cloud. The cloud climbs in response to its increasing buoyancy as the negatively buoyant droplets fall out.

of small, long-lived droplets from the cloud at speeds as low as 0.06 m s^{-1}. This settling speed and time to complete evaporation are consistent with pure water droplets smaller than 50 μm diameter that have a settling speed of less than 0.068 m s^{-1} and time to complete evaporation of less than 6 s (Holterman 2003). Smaller settling speeds were also observed, but difficult to estimate owing to their irregular motion.

Figure 7 illustrates the physical picture that emerges from a synthesis of our flow visualizations, prior work on cloud visualization using schlieren (e.g. Tang *et al.* 2009) and droplet sampling (e.g. Morawska *et al.* 2009*b*). Violent respiratory events release droplet-bearing turbulent momentum puffs of moist, buoyant air ejected in a direction that depends on the individual. As the buoyant momentum puff advances, it entrains ambient air, its width increasing and its speed decreasing with distance from

the source (Turner 1979) as illustrated in figure 1(*a*,*b*). While large droplets follow a ballistic trajectory largely unaffected by the turbulent cloud, smaller droplets may remain suspended in the cloud and are circulated therein until they settle out. In § 4.2 we first describe the fate of suspended droplets using a discrete fallout model, where drops remain suspended in the cloud until their settling speeds match the speed of the cloud. A more sophisticated fallout description is then developed that accounts for a continuous fallout of the droplets along the entirety of the cloud's trajectory. Such dynamics are illustrated for horizontally directed flows in figure 7.

3. Analogue experiments

As an experimental analogue to droplet-laden coughs and sneezes, we examined the dynamics of turbulent, dyed, particle-laden fluid injected into a quiescent water tank from a piston (figure 8). The cloud buoyancy resulted from the use of salty water in the tank and fresh water in the payload (see table 1). The water tank of height 60 cm, length 3.25 m and width 85 cm was divided into two parts, a release section of approximately 75 cm in length that contained the source piston, and an illuminated observation section of approximate length 2.5 m. A wall was used to separate the two regions in order to minimize disturbances to the observation area caused by the piston release. The piston was placed 23 cm above the base of the tank, which minimized wall and surface effects on the puff trajectory, such as attraction to the boundary via the Coanda effect. The piston, with internal radius 2.6 cm and opening diameter of 0.9 cm, was filled and its payload (88 cm^3) released over a characteristic time of 375 ± 50 ms. This was fine-tuned to minimize the release time while still maintaining a puff subsequent cloud dynamics. During release, the Reynolds number of the fluid payload was approximately 5000. The trajectory of the resulting turbulent puff cloud and the deposition pattern of its particles were recorded with a Nikon SLR D90 camera at 24 f.p.s. A backdrop of black felt was used to minimize reflections from the tank wall.

Three dozen experiments were carried out, five of which are detailed here (I–V see table 2). One experiment (I) involved a buoyant puff cloud free of beads, while the other experiments (II–V) involved bead-laden buoyant clouds. The settling speed of the particles was measured in fresh water. The difference in density between the fresh dyed water contained in the piston and the clear water of the tank ranged from 5.4 to 10 mg cm^3. The tank fluid density was measured using a densitometer (DMA 35N, Anton Paar) at several different locations in the tank in order to ensure that it was well-mixed. Care was taken to ensure that residual disturbances caused by the filling process dissipated before release. Note that data acquisition ceased when the buoyant puff approached the bottom or the top of the water tank. In addition, some of the clouds grew asymmetrically; which can be attributed to residual motion originating from the release mechanism, for example, the formation of an asymmetric vortex ring at the front of the cloud (e.g. Scorer 1957). Such experiments were discarded from consideration.

As the cloud progresses, the ambient fluid is entrained and mixes with the cloud, leading to an increase in size and hence a deceleration of the puff (Turner 1979). The entrainment of ambient fluid modifies the total mass and volume, but the cloud roughly retains its shape. The self-similar growth of the turbulent puff leads to $r = \alpha s$, where r is the half-width of the cloud and s the distance from the source (see figure 1*a*). In reality, details of source conditions displace the effective origin of the cloud relative to the piston (Hunt & Kaye 2001). The virtual origin can be computed by extrapolating the measured r against s plot, as illustrated in figure 7.

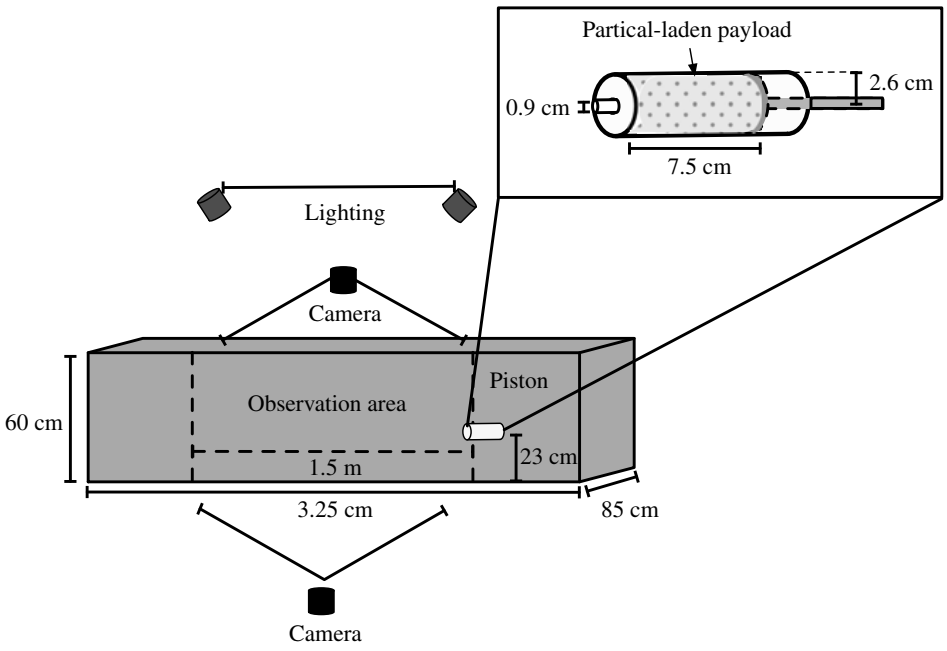

FIGURE 8. A schematic illustration of our analogue experiment, conducted in a tank containing salty water. Buoyant, dyed, particle-laden payloads were released using the rapid triggering of the piston. The release and observation regions were separated by a wall to minimize disturbances to the particle-laden puff by the piston release.

	I	II	III	IV	V
N	0	252	935	4200	1258
d (mm)	—	2.86 ± 0.04	1.36 ± 0.04	0.78 ± 0.08	0.46 ± 0.04
ρ_p (g cm^{-3})	—	2.4	2.4	2.5	2.5
u_s^m (cm s^{-1})	—	35.5 ± 0.5	22 ± 0.5	11.3 ± 0.5	6.6 ± 0.25
u_s^t (cm s^{-1})	—	32.3	19.3	11.8	6.65
Re_p	—	934	270	92	30
ϕ	0	3.51×10^{-2}	1.4×10^{-2}	1.19×10^{-2}	7.3×10^{-4}
ρ_{tank} (g cm^{-3})	1.0029	1.0050	1.0050	1.0053	1.0096
ρ_f (g cm^{-3})	0.999 75	0.999 55	0.999 55	0.9995	0.999 55
v_0 (m s^{-1})	1.007	1.007	1.174	1.118	1.102
B_0 (kg m s^{-2})	2.72×10^{-3}	-3.77×10^{-2}	-1.22×10^{-2}	-1.04×10^{-2}	7.73×10^{-3}
I_0 (kg m s^{-1})	8.86×10^{-2}	9.29×10^{-2}	1.05×10^{-1}	1×10^{-1}	9.70×10^{-2}

TABLE 1. Parameters used in experiments I to V: number of beads N, bead diameter d, bead density ρ_p, measured settling speed u_s^m, theoretical settling speed u_s^t, and associated particle Reynolds number $Re_p = u_s^t d/\nu$, where ν is a water kinematic viscosity. Here, ϕ is the initial volume fraction of particles in the payload of volume 88 cm^3. We also report the density of the tank water ρ_{tank} and fluid released ρ_f, as well as initial cloud velocity v_0, momentum I_0 and buoyancy B_0. The dynamic viscosity of water is $\mu = \rho\nu = 1.002 \times 10^{-3}$ kg m^{-1} s^{-1}.

While these clouds are buoyant, they are initially driven by momentum, as is the case for coughs and sneezes. Two phases of the cloud evolution were apparent in all experiments. The first phase is dominated by a jet-like dynamics, corresponding to

	α_1	α_2	α_{avg}	x_T (cm)	x^t_{fall} (cm)	x^t_{max} (cm)	x^o_{max} (cm)
I	0.166 ± 0.01	0.028 ± 0.006	$0.089 < 0.097 < 0.105$	25	—	—	—
II	0.10 ± 0.01	0.034 ± 0.003	$0.063 < 0.07 < 0.075$	35	22 ± 2	29 ± 3	31
III	0.13 ± 0.022	0.018 ± 0.003	$0.061 < 0.074 < 0.0856$	35	37 ± 6	41 ± 6	37
IV	0.10 ± 0.007	0.02 ± 0.003	$0.057 < 0.061 < 0.066$	25	57 ± 4	60 ± 4	63
V	0.134 ± 0.003	0.021 ± 0.0029	$0.075 < 0.077 < 0.08$	19	63 ± 2	65 ± 2	66

TABLE 2. Entrainment coefficients measured in the two phases of the cloud dynamics in each experiment: in the jet phase α_1, in the puff phase α_2, and their average α_{avg}. Here, x_T is the observed distance of transition from the jet to puff phases extracted from the cloud trajectory and size data (e.g. figure 9). Here, x^t_{fall} is the predicted fallout distance of particles from the cloud. Here, x^t_{max} is the predicted maximum distance of deposition of particles (or range). Finally, x^o_{max} is the observed maximum distance of deposition of the particles at the bottom of the tank. All theoretical predictions are computed using α_{avg}.

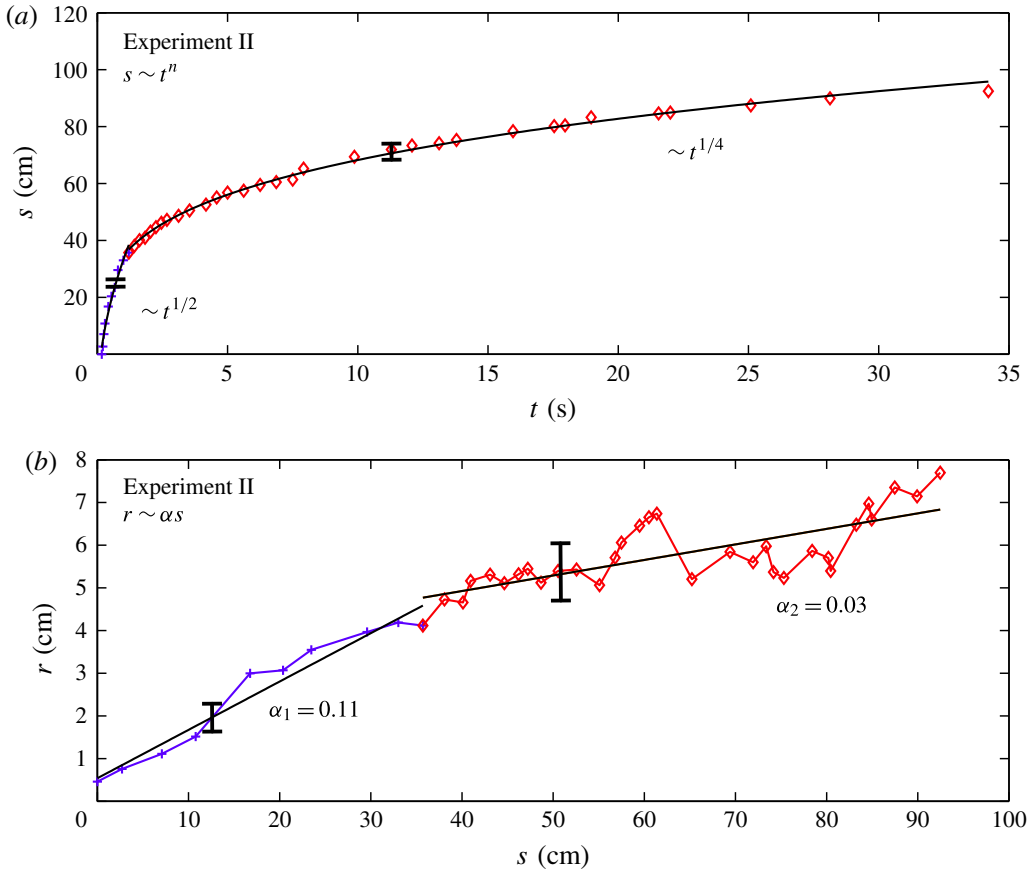

FIGURE 9. (Colour online) (*a*) Relationship between the distance travelled by the cloud's geometric centre s and the time t for experiment II. (*b*) Relationship between distance s travelled and the mean radius of the puff cloud r for experiment II. Note that the observed transition in slope is common to all experiments I–V. The slopes are used to determine entrainment coefficients in the first jet phase α_1 and in the second puff phase α_2, as reported in table 2. Characteristic error bars are shown at different stages.

the high-speed release of the payload. The second phase is dominated by a puff-like dynamics, which is characterized by the self-similar growth of the puff cloud. For a jet, the conservation of momentum flux $M_0 \sim \rho r^2 (\mathrm{d}s/\mathrm{d}t)^2$ combined with the self-similar growth of the cloud $r \sim \alpha s$ leads to $\mathrm{d}s/\mathrm{d}t \sim 1/s$; hence, $s \sim t^{1/2}$. For a puff, the conservation of momentum $I_0 \sim \rho r^3 \, \mathrm{d}s/\mathrm{d}t$ combined with the self-similar growth of the cloud $r \sim \alpha s$ leads to $\mathrm{d}s/\mathrm{d}t \sim 1/s^3$; hence, $s \sim t^{1/4}$. Distinct jet and puff phases were apparent in all our experiments.

Figure 9 illustrates the dependence of the position s on time t and the corresponding dependence of r on s. The change of slope in the relationship between r and s indicates the transition between the jet and puff regimes and the associated change in entrainment coefficient α. Similar changes of slope and scalings were observed for all experiments. The entrainment coefficient of each phase was extracted and reported as α_1 and α_2 in table 2. Here, x_T, the distance of transition from the jet to puff phases, is also given. The range of coefficients measured is $0.09 < \alpha_1 < 0.18$ for the jet phase and $0.015 < \alpha_2 < 0.037$ for the puff phase (see table 2). Reported values of α for thermals ranged from 0.2 to 0.34 with a mean of 0.25 (Scorer 1957) or from 0.13 to 0.53 (Richards 1961). Richards (1965) showed that non-buoyant puffs and thermals

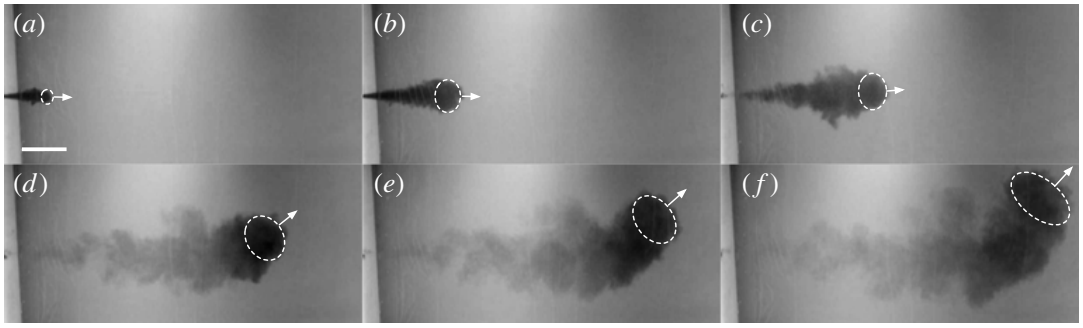

FIGURE 10. Illustration of the tracking of the front and geometric centre of the turbulent cloud in experiment I as it moves away from the source. The successive images are taken at times (*a*) 0.08 s, (*b*) 0.3 s, (*c*) 0.46 s, (*d*) 1.54 s, (*e*) 2.25 s and (*f*) 3.5 s after release. Scale bar, 10 cm.

are similar, with α ranging from 0.15 to 0.58. Richards (1965) noted that there is a larger variability in the entrainment coefficient of puffs than thermals.

Figure 11 shows the trajectory of the buoyant puff cloud released without beads (experiment I). The inset shows the superposition of images tracing the shape of the cloud as it grows away from the source. The front edge and shape of the cloud were tracked on the video frames. As was observed in both our experiments and previous studies of thermals, the cloud was best described as an ellipsoid (Scorer 1957). The tracking of the position of the geometric centre of the cloud (figure 10) was used to construct the time evolution of its position s. Note that in the inset and snapshots of figures 10–11, the upturn in the cloud is evidence of the influence of buoyancy on the cloud motion.

Figure 12 shows the trajectories of the puff cloud when beads are contained in the payload. Note that the addition of beads modifies the dynamics of the cloud, decreasing the entrainment coefficient and so increasing the particle range. Quite generally, turbulence affects the mixing and coalescence of suspended particles and droplets in various multiphase flows (Ghosh *et al.* 2005). The best fit entrainment coefficient for the multiphase cloud was lower than for homogeneous clouds as is consistent with the recent observations of Lai *et al.* (2013). Indeed, figure 12 shows that the trajectories of the clouds II–V are best captured by the average of the jet and puff phase entrainment coefficients α_{avg}. The average values all fall close to 0.07, the value reported by Lai *et al.* (2013) in their study of a two-phase sediment cloud.

The pattern of bead deposition is shown in figure 13. Such images were analysed to extract the maximum distance of deposition, their range x^o_{max}.

4. Theoretical model

We proceed by developing a theoretical model based on the physical picture of violent expiratory events as discrete emissions of droplet-laden multiphase turbulent clouds (figure 7). This model is used to rationalize the role of the multiphase cloud in extending the observed range of the beads reported in our analogue experiments and to yield insight into real coughs and sneezes.

Recall that the expiratory puff is treated as an isolated mass of turbulent fluid moving through an undisturbed environment, driven initially primarily by its momentum rather than its buoyancy; hence, it is initially closer to a multiphase

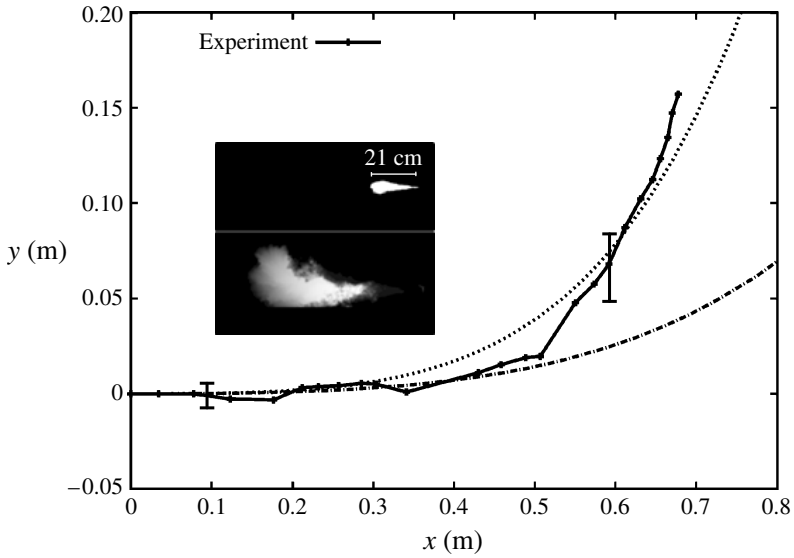

FIGURE 11. Trajectory of the turbulent buoyant puff cloud for experiment I, where no beads are included. The insets show the superposition of the images of the shape of the cloud upon release (at the end of the jet phase), followed by the superposition of the images retracing the full evolution of the cloud. The recorded trajectory is compared with the theoretical predictions (based on (4.7)–(4.11)) obtained using the jet entrainment coefficient $\alpha_1 = 0.17$ (dashed line) as the upper bound and the average entrainment coefficient $\alpha_{avg} = 0.08$ (dot-dashed line) as the lower bound. Both coefficients were measured from our experiments (see table 2).

puff than a thermal. However, buoyancy cannot be entirely neglected and ultimately influences the cloud trajectory as is evident in figure 5. Hence, we model the cloud as a buoyant multiphase puff with initial buoyancy B_0 and initial momentum I_0. For a one-phase cloud without suspended particles, the cloud buoyancy is defined as $B = V_c(\rho_a - \rho_c)g$, where V_c and ρ_c are the volume and density of the cloud, respectively. Here, ρ_a is the density of the ambient air and g the acceleration due to gravity (see figure 4*h*). If the cloud has initial momentum I_0 and buoyancy B_0, one expects a transition from momentum to buoyancy dominated dynamics at a time $t* = I_0/B_0$. In our analogue experiments, particles generally fall out prior to such a transition; however, small droplets may remain suspended in real cough and sneeze clouds throughout their evolution.

We model the multiphase flow with initial density

$$\rho_c(0) = \sum_{n=1}^{N} (\rho_p - \rho_f)\phi_n(0) + \rho_f, \tag{4.1}$$

where $\phi_n(0)$ is the volume fraction of suspended material, specifically, the droplets or particles of diameter d_n, i.e. $N_n v_n/V$, where $v_n = \pi d_n^3/6$ is the drop volume, V the cloud volume, and N_n is the number of drops or particles suspended in the cloud of diameter d_n. The cloud moves forward, entraining ambient fluid of density ρ_a and acquiring a volume $V(t) = V(0) + V_a(t)$ provided the drops remain suspended in the cloud. Note that the initial volume fraction of the fluid phase in real coughs and sneezes reported previously is relatively small, e.g. 10^{-5} (Duguid 1946), or

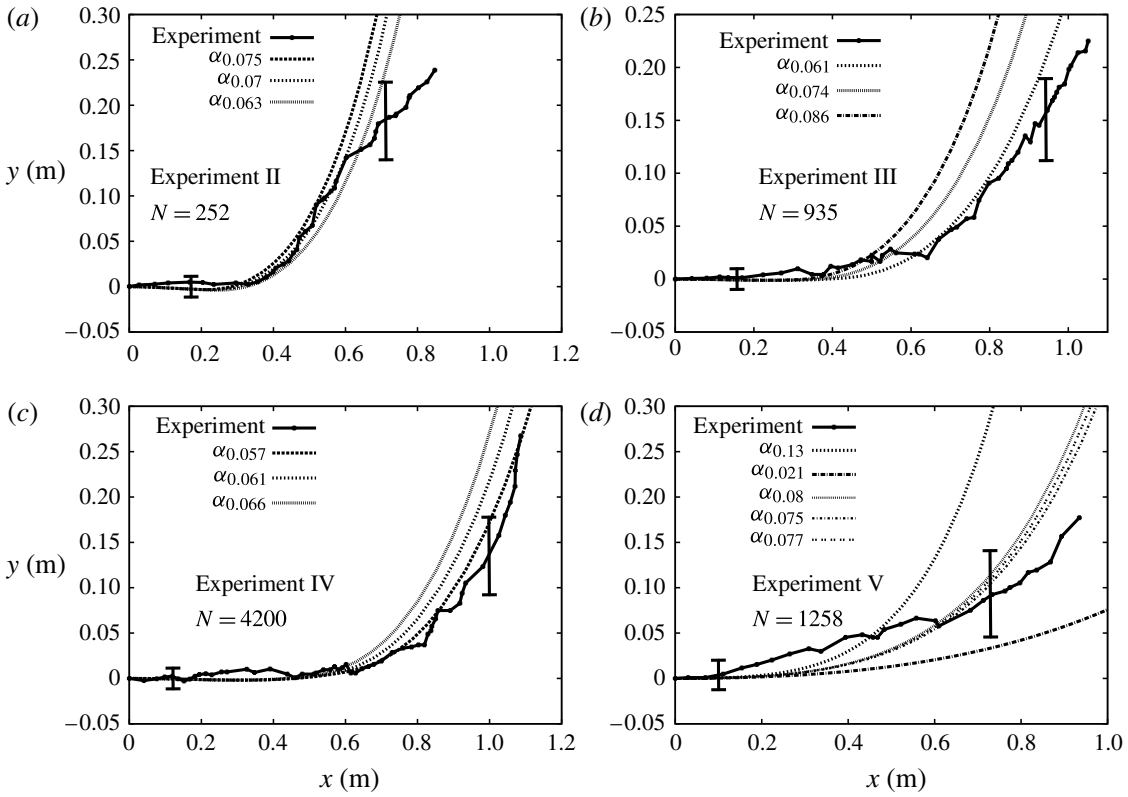

FIGURE 12. Trajectories of the buoyant multiphase puff clouds of experiments II–V. The theoretical cloud trajectories based on (4.7)–(4.11) obtained with the range of entrainment coefficients displayed in both the figures and in table 2 are shown against the observed experimental trajectories. The number N of particles used for each experiment is also displayed, their properties being listed in table 1.

even less, e.g. 10^{-7} (Johnson *et al.* 2011). The low volume fraction ($\ll 1\,\%$) allows us to neglect the modifications to the droplet speeds required at higher particle concentration (Blanchette 2003).

The cloud density evolves according to

$$\rho_c(t) = \frac{V(0)}{V(t)}\rho(0) + \rho_a\left(1 - \frac{V(0)}{V(t)}\right), \tag{4.2}$$

or alternatively

$$\rho_c(t) = \frac{V(0)}{V}(\rho_f - \rho_a) + \rho_a + \sum_{n=1}^{N}\phi_n(t)(\rho_p - \rho_f), \tag{4.3}$$

where the volume fraction of suspended material of diameter d_n at time t is $\phi_n(t) = N_n(t)v_n/V$. We consider the case where all of the suspended material has the same density ρ_p. Within this framework, droplets or particles remain suspended within the puff until their settling speed u_{sn} exceeds the mean circulation speed within the puff. As the puff speed necessarily decreases with distance from the source, so does the size of the suspended material: the largest drops fall out of the cloud directly after ejection, while the smallest drops and droplet nuclei can remain suspended within the puff for a significant distance.

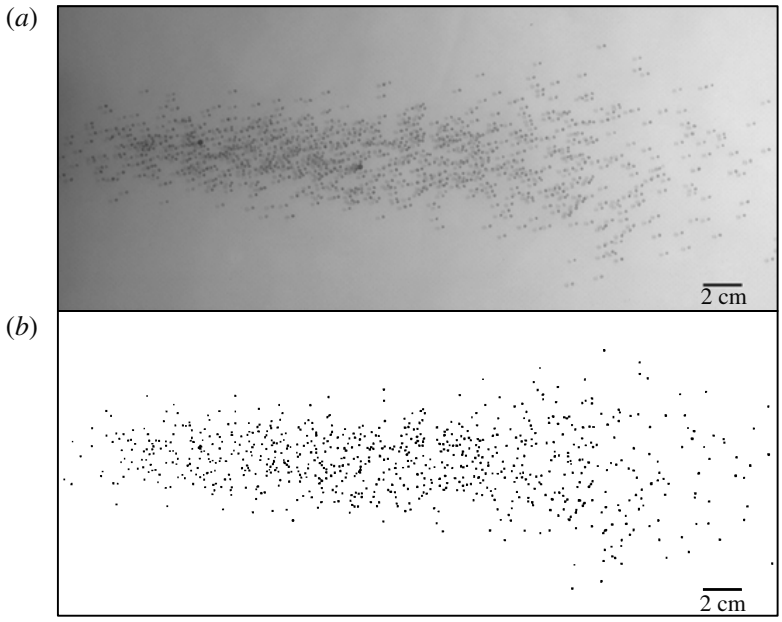

FIGURE 13. Deposition pattern of beads in experiment III. We show (*a*) the original image and (*b*) the treated image from which the particle counting and estimation of maximum particle range is obtained. Here, the maximum observed deposition range is $x^o_{max} = 37$ cm, as listed in table 2.

4.1. *Trajectory*

The trajectory of the puff is governed by the evolution of its momentum I and buoyancy B. The buoyancy force is vertical, causing the cloud to follow a curvilinear trajectory denoted by (s, θ) as illustrated in figure 1(*b*). The equations of motion for the cloud are decomposed into horizontal x and vertical y components. The horizontal and vertical momentum; $I_x = |I| \cos\theta$ and $I_y = |I| \sin\theta$, evolve according to

$$\frac{\mathrm{d}|I| \cos\theta}{\mathrm{d}t} = 0, \quad \frac{\mathrm{d}|I| \sin\theta}{\mathrm{d}t} = B(t), \tag{4.4}$$

where

$$|I| = \rho_c \eta r^3 \frac{\mathrm{d}s}{\mathrm{d}t} = \rho_c \eta \alpha^3 s^3 \frac{\mathrm{d}s}{\mathrm{d}t}. \tag{4.5}$$

Here, $B(t) = V_c(t)(\rho_a - \rho_c(t))g$ is the cloud buoyancy, $\mathrm{d}s/\mathrm{d}t = w$ is the mean speed of the cloud along its curvilinear trajectory, $V = \eta r^3 = \eta \alpha^3 s^3$ is the cloud volume (see figure 1) and $|I|^2 = I_x^2 + I_y^2$. Equation (4.4) can be solved given initial conditions, $I_x(0) = I_0 \cos\theta_0$, $I_y(0) = I_0 \sin\theta_0$, $B(0)$, $V(0) = V_0$, $s(0) = s_0$, $|I|(0) = I_0$ and $\theta = \theta_0$.

Note that if the cloud is spherical, $\eta = 4\pi/3$; however, it has been observed in both our experiments and previous studies of thermals that the cloud is better described as an ellipsoid with radius r and height kr, leading to $\eta = k4\pi/3$ with $k = 9/(4\pi)$ (Scorer 1957). Hence, the volume of the cloud can be expressed as $V = 3\alpha^3 s^3$. This form is used throughout the remainder of the paper and is consistent with the observations and developments of Scorer (1957).

The total mass of the cloud increases through entrainment according to $\mathrm{d}(\rho_c V)/\mathrm{d}t = \eta \rho_a \alpha^3 s^2 (\mathrm{d}s/\mathrm{d}t)$. If ρ_a is constant, then necessarily $\mathrm{d}B/\mathrm{d}t = 0$: entraining fluid with no

buoyancy does not change the cloud buoyancy. The conservation of initial buoyancy $B(0) = B_0$, which is valid prior to particle fallout leads to the following simplification of (4.4):

$$I_x = |I| \cos\theta = I_0 \cos\theta_0 \quad I_y = |I| \sin\theta = B_0 t + I_0 \sin\theta_0. \tag{4.6}$$

In this case, $|I|^2 = I_x^2 + I_y^2$ and (4.5) leads to

$$\frac{\mathrm{d}s}{\mathrm{d}t} = \frac{\left(B_0^2 t^2 + I_0^2 + 2I_0 B_0 \sin\theta_0 t\right)^{1/2}}{\eta \alpha^3 \rho_c s^3}. \tag{4.7}$$

Using (4.3), equation (4.7) becomes

$$\frac{\mathrm{d}s}{\mathrm{d}t} = \frac{\left(B_0^2 t^2 + I_0^2 + 2I_0 B_0 \sin\theta_0 t\right)^{1/2}}{Z_p + \eta \alpha^3 \rho_a s^3}, \tag{4.8}$$

where

$$Z_p = V_0(\rho_f - \rho_a) + V_p(\rho_p - \rho_f) \quad \text{with } V_p = \sum_{n=1}^{N} N_n v_p. \tag{4.9}$$

The governing equation for $\theta(t)$ can also be obtained by manipulation of (4.6):

$$\tan\theta = \frac{B_0}{I_0 \cos\theta_0} t + \tan\theta_0. \tag{4.10}$$

After some algebra, the trajectory of the cloud (s, θ) can be written in the form:

$$[Z_p s + \eta \rho_f s^4/4] = \frac{I_0^2}{2B_0} \left\{ \frac{\tan\theta}{\cos\theta} + \ln\left[\tan\theta + \frac{1}{\cos\theta}\right] \right\} \quad \text{and} \quad \theta = \arctan\left[\frac{B_0 t}{I_0}\right], \tag{4.11}$$

with initial conditions $(s_0, \theta_0) = (0, 0)$ at $t_0 = 0$. Note that this result breaks down for vertical trajectories, that is, when $\theta = \pm\pi/2$.

4.2. *Fallout*

As the cloud entrains fluid and decelerates, its mean velocity eventually becomes comparable to the settling speed of the largest suspended droplets. We first describe the particle fallout as being discrete, assuming that droplets fallout when their settling speed matches the mean speed of the cloud $\mathrm{d}s/\mathrm{d}t$, which corresponds to its characteristic internal circulation speed. The Stokes settling speed $u_s = gd^2/(18\mu)(\rho_p - \rho_a)$ was previously used to describe the settling of droplets emitted by violent expirations (e.g. Wells 1934, 1955). However, a more general formulation is required to describe the large size range of droplets and droplet nuclei. Specifically, inertial effects are important for large droplets, while the shortcomings of the non-slip hypothesis becomes important for particles smaller than 1 μm (Hinds 1999; Crowder *et al.* 2001; Lauga, Brenner, & Stone 2005). Porosity of the residual droplet nuclei in real coughs and sneezes can also substantially affect their settling speeds (e.g. Kajihara 1971; Edwards *et al.* 1998; Crowder *et al.* 2001). The dependence of the settling speed u_s on drop size is characterized in the Appendix.

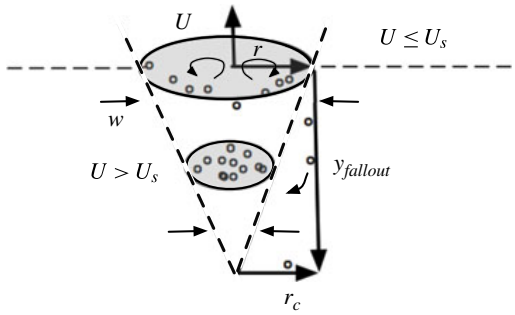

FIGURE 14. (Colour online) Schematic of the spreading and settling of the particles from a cloud emitted vertically, which is roughly analogous to flows generated by patients sneezing or coughing upward while lying down in a hospital setting. A particle may remain suspended in the cloud until its settling speed U_s exceeds the speed of the decelerating cloud U. The fallout height $y_{fallout}$ and range of contamination r_c are both indicated and would be given by the smallest positive root of (4.13).

4.2.1. *Discrete fallout*

For discrete particle fallout, the fallout criterion of droplets or particles of diameter d is thus $U_s = \mathrm{d}s/\mathrm{d}t$. In the simplified case of a vertical buoyant puff (see figure 14), with the initial condition $\theta_0 = \pi/2$, the governing equations become

$$\frac{\mathrm{d}s}{\mathrm{d}t} = \frac{\mathrm{d}y}{\mathrm{d}t} = \frac{B_0 t + I_0}{Z_p + \rho_a \eta \alpha^3 y^3}. \tag{4.12}$$

Here, the fallout criterion $U_s = \mathrm{d}y/\mathrm{d}t$ leads to the following polynomial equation for the fallout height y

$$-\frac{(\eta U_s \rho_a \alpha^3)^2}{2B_0} y^6 + \frac{\rho_a \eta \alpha^3}{4} y^4 - \frac{U_s^2 Z_p \eta \alpha^3 \rho_a}{B_0} y^3 + Z_p y + [I_0^2/(2B_0) - (U_s Z_p)^2/(2B_0)] = 0. \tag{4.13}$$

The smallest positive root determines the height and time of fallout for droplets with settling speed U_s. For the horizontal configuration (figure 7) the derivation is analogous; however, the fallout criterion leads to a transcendental equation rather than a polynomial.

We first assume that, following fallout from the cloud, the particles of diameter d are in free fall with initial position $(s_{fall}(t_{fall}), \theta_{fall}(t_{fall}))$ or (x_{fall}, y_{fall}) and exit velocity $(U_s \cos\theta_{fall}, U_s \sin\theta_{fall})$. While the fallout time and position are important, the horizontal range of deposition (x_{range}) is of primary interest for disease transmission by emitted pathogens. We report in table 2 the theoretically predicted fallout distance x^t_{fall} and the maximum distance of deposition (or range) x^t_{max}. The latter is computed using the free fall equations with the initial conditions prescribed by fallout at x^t_{fall}, specifically, $u = u(x^t_{fall}, y^t_{fall}, t^t_{fall})$. The predicted range x^t_{max} is compared with that observed x^o_{max} in our analogue experiments.

We have thus far assumed that the particles or droplets remain in the cloud until the mean cloud velocity and so its internal speed of recirculation matches the settling speed of the particles. This implicitly assumes that the recirculation within the cloud is acting to suspend particles. We note that such is not the case at the edge of the cloud

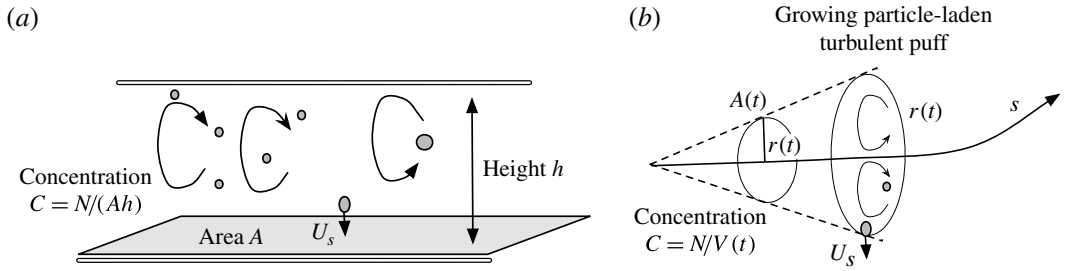

FIGURE 15. (*a*) Schematic illustration of sedimentation from a turbulent ambient as described by Martin & Nokes (1988). Particles with settling speed less than the characteristic turbulent speed remain suspended unless they settle into the lower boundary layer. The result is a suspended particle concentration that decays exponentially over a timescale h/U_s. (*b*) Schematic of our model of continuous fallout as described by the system (4.15)–(4.20). Particles now settle out of the cloud continuously prior to the final fallout time, $t_{fallout}$, as predicted by the discrete fallout model.

where the recirculation is largely horizontal. Consequently, the droplets can leave the cloud before reaching the fallout length, as is consistent with our observations of a relatively continuous deposition of particles in our analogue experiments (figure 13). We thus modify our discrete fallout model through considering the change in buoyancy and volume of the turbulent puff associated with continuous particle settling.

4.2.2. *Continuous fallout*

Martin & Nokes (1988) proposed a simple model to describe particle settling through a turbulent fluid in a bounded container. They assume that the fluid is well mixed and turbulent and that the particle settling speed is substantially less than the characteristic turbulent speed. The particles thus remain suspended unless they settle into the lower boundary layer, in which case they sediment out. Their model predicts an exponential decrease of the particle concentration with a timescale of h/U_s, where h is the height of the bounded container and U_s is the settling speed of the suspended particles (see figure 15). Blanchette (2003) applied this model to describe the sedimentation of bidisperse particles from riverine gravity currents, a model further developed by Clarke, Bush & Bush (2009). Following such ideas, we propose a model of continuous particle fallout, in which particles settle out continuously from the cloud prior to final fallout.

Based on our observations (see also Lee *et al.* 2013), we assume that the settling of particles occurs through the lower half surface of the turbulent puff cloud with area $A(t)/2$. This gives the rate of change of the number of particles within the cloud:

$$\frac{\mathrm{d}N}{\mathrm{d}t} = -U_s A(t) C(t)/2. \tag{4.14}$$

Assuming that the particles are homogeneously mixed within the cloud, the particle concentration $C = N(t)/V(t)$; hence, we obtain

$$\frac{\mathrm{d}N}{\mathrm{d}t} = -\frac{3U_s N}{2\alpha s}, \tag{4.15}$$

where we used our previous expressions for the volume and surface area of the cloud, $V(t) = \eta\alpha^3 s(t)^3$ and $A(t) = 3\eta\alpha^2 s(t)^2$. Unlike in the model of Martin & Nokes (1988),

the volume and surface area of the cloud is changing due to entrainment. We can nevertheless solve for the deposition pattern and its effect on the trajectory of the cloud by complementing (4.15) with the following system of coupled differential equations:

$$\frac{\mathrm{d}V}{\mathrm{d}t} = 3\eta\alpha^3 s^2 \frac{\mathrm{d}s}{\mathrm{d}t} - v_p \frac{\mathrm{d}N}{\mathrm{d}t} \tag{4.16}$$

$$\frac{\mathrm{d}\rho_c}{\mathrm{d}t} = \frac{1}{V}\left[v_p \frac{\mathrm{d}N}{\mathrm{d}t}(\rho_c - \rho_p) + 3\eta\alpha^3 s^2 \frac{\mathrm{d}s}{\mathrm{d}t}(\rho_a - \rho_c)\right] \tag{4.17}$$

$$\frac{\mathrm{d}B}{\mathrm{d}t} = g\rho_a \frac{\mathrm{d}V}{\mathrm{d}t} - g\frac{\mathrm{d}(V\rho_c)}{\mathrm{d}t} \tag{4.18}$$

$$\frac{\mathrm{d}I_y}{\mathrm{d}t} = B \tag{4.19}$$

$$\frac{\mathrm{d}s}{\mathrm{d}t} = \sqrt{I_y^2 + (I_0 \cos\theta_0)^2/(V\rho_c)}, \tag{4.20}$$

where the cloud density ρ_c is defined in (4.2) and depends explicitly on the particle concentration. We can then use the system (4.15)–(4.20) to derive the trajectory of the cloud prior to $t_{fallout}$ and predict the associated particle range x^t_{max}. The latter quantities can be obtained for either of our two fallout models, with fallout happening either instantaneously at t_{fall} or continuously prior to t_{fall}.

The predicted behaviour of the particle-bearing multiphase buoyant cloud is now compared with the experimental observations. The trajectories of the clouds in figures 11 and 12 are compared with our theoretical prediction obtained using the range of entrainment coefficients recorded in table 2. The comparison between predictions of the discrete and continuous fallout models is shown in figure 16. The theoretically predicted fallout distance x^t_{fall} and the maximum distance of deposition (or range) of the particles x^t_{max} are given in table 2 and compared with the observed maximum distance of deposition x^o_{max} (e.g. figure 13) for each experiment also in table 2. Note that, except for the larger beads used in experiment II, beads fell out of the cloud in the puff phase. The comparisons of x^o_{max} and x^t_{max} show a satisfactory agreement between experiments and theory for the bead deposition range. We also see that the multiphase cloud substantially increases the range of the beads. Indeed, using a simple ballistic calculation (in which drag is neglected), one obtains upper bounds for the maximum deposition distance of 21, 25, 24 and 24 cm from the source for the experiments II, III, IV and V, respectively. Accounting for drag reduces these values to 4, 2, 1 and 0.5 cm, respectively. The multiphase cloud dynamics extends these ranges to 31, 37, 63 and 66 cm, respectively (see table 2), i.e. by a factor of up to 130 for the smallest beads. Our theoretical model of a turbulent multiphase cloud with continuous fallout rationalizes this observed increase of range, which is most pronounced for smaller particles more readily suspended by the cloud.

5. Application to clinical data

Our combined experimental and theoretical study has shown how particles can be suspended in turbulent clouds, their range thus being extended. We now consider the implications of these findings for real coughs and sneezes. Cough clouds initially contain both buoyant gas and negatively buoyant droplets. We proceed by using our model to describe their dynamics using the initial parameters of coughs recorded in the clinical literature. Initial velocity, opening angle, moisture, volume and other

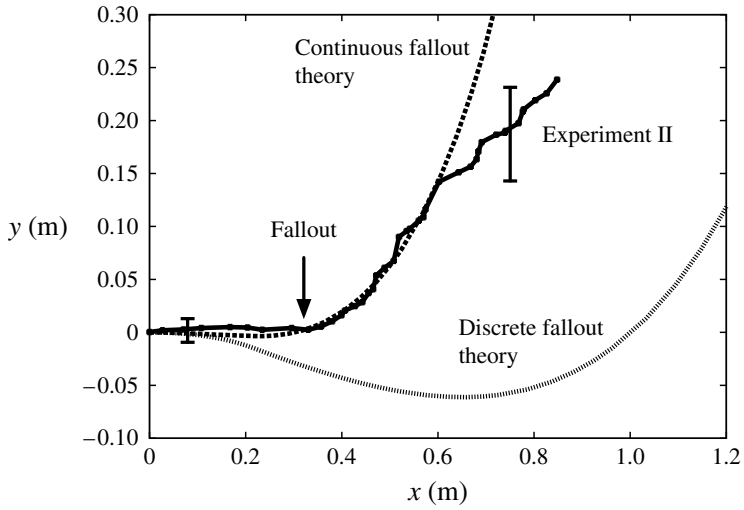

FIGURE 16. Comparison of observed cloud trajectory (experiment II) and trajectories predicted on the basis of our discrete and continuous fallout models with entrainment coefficient $\alpha_{avg} = 0.07$. The observed point of final bead fallout is indicated. Note that the dip in the trajectory predicted by the discrete fallout model is due to its underestimating the cloud buoyancy through neglect of the continuous fallout of negatively buoyant particles.

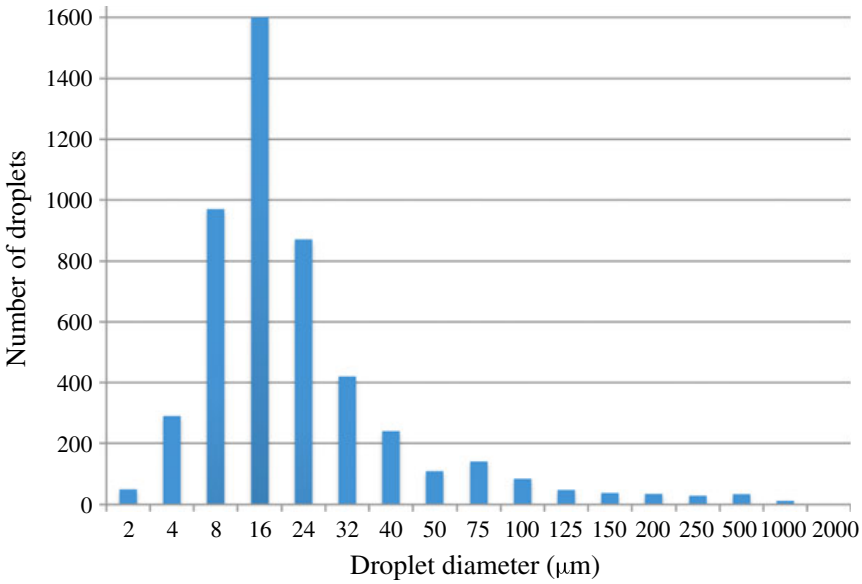

FIGURE 17. (Colour online) Histogram of droplet size in coughs (reproduced from Duguid 1946).

parameters recorded for clinical coughs are taken from various sources (see table 3). The droplet size distribution considered is that reported by Duguid (1946) (figure 17).

Figure 18(*a*,*b*) show the trajectories of two multiphase buoyant clouds predicted by the theoretical models developed in § 4. Figure 18(*a*) shows the trajectory and fallout distance of a multiphase cough cloud composed of large droplets of diameter 700 μm, while 18(*b*) illustrates the same for a cloud with droplets of diameter

T_f	34 °C with 23 °C ambient	Höppe (1981)
	30–35 °C in mouth and nose	Morawska *et al.* (2009*a*)
RH_f	85 %	McCutchan & Taylor (1981)
	85–100 %	Morawska *et al.* (2009*a*)
ρ_f air exhaled	0.98 kg m^{-3}	Picard *et al.* (2008)
ρ_d droplets	993 kg m^{-3} in ambient at 34 °C	Nicas *et al.* (2005)
V	1.2 l	Gupta *et al.* (2009)
	Estimated over 100 coughs	
u	Mean of 11.2 m s^{-1}	Gupta *et al.* (2009), Tang *et al.* (2009)
α	0.2116	Tang *et al.* (2009)
	From opening angle $\theta = 23.9 \pm 3.4°$	

TABLE 3. Characteristics of a typical cough. Parameters include the temperature of the fluid exhaled T_f, its relative humidity RH_f and the resulting density ρ_f computed using the evaporation model of Picard *et al.* (2008). The ambient air density $\rho_a = 1.172$ kg m^{-3} for typical winter conditions (temperature 23 °C, relative humidity 19.1 %). The dynamic viscosity of air is 1.9×10^{-5} kg s^{-1} m^{-1}. The density of the droplets emitted ρ_d, the total volume of a cough fluid V, its mean initial velocity u, and its entrainment coefficient are estimated based on the opening angle of the cough cloud α. The initial volume fraction of droplets used is $\phi = 1.89 \times 10^{-7}$, with initial momentum $I_0 = 1.31 \times 10^{-2}$ kg m s^{-1} and buoyancy $B_0 = 2.3 \times 10^{-3}$ kg m s^{-2}.

30 μm. Note that the height reached for the cloud containing 30 μm droplets is comparable to ceiling heights (4–6 m) of most facilities where ventilation systems reside. Figure 18(*c*) shows the mean speed of the cough cloud decaying with time (and distance) from the source. The settling speeds of droplets of size 30–700 μm are also compared with the mean speed of the cloud, yielding the fallout time of each droplet group. We assume that upon leaving the cloud, the droplets or particles have the velocity and position of the cloud at fallout. The resulting distance at which the droplets reach the floor (estimated at 2 m below the cougher's mouth) can thus be computed.

The fallout and contamination ranges are compared in figure 18(*d*). We see again that the cloud dynamics plays an important role in extending the range of all droplets, particularly the smallest ones. Indeed, without the cloud entrainment, the trajectory of the droplets of diameter $d \leqslant 100$ μm expelled at cough cloud velocity would only be up to a dozen centimetres away from the mouth. This range is extended to metres away from the cougher by the cloud entrainment. For example, figure 18(*b*) shows that droplets of diameter 30 μm can have a horizontal range of up 2.5 m away from the cougher due to cloud dynamics. Moreover, when relatively large particles are ejected in the forward direction from the cloud, their range can be extended significantly. Indeed, their higher exit velocities relative to smaller drops that fall out later can lead to a non-monotonic variation of the contamination range as a function of the droplet diameter, as indicated in figure 18(*d*).

6. Summary and conclusion

We have examined the factors that influence the transport of droplet-borne pathogens in violent respiratory expirations. We have presented experiments of human coughs and sneezes, which demonstrate that violent respiratory flows are turbulent, multiphase puffs. We observed that the initial emitted turbulent fluid entrains ambient

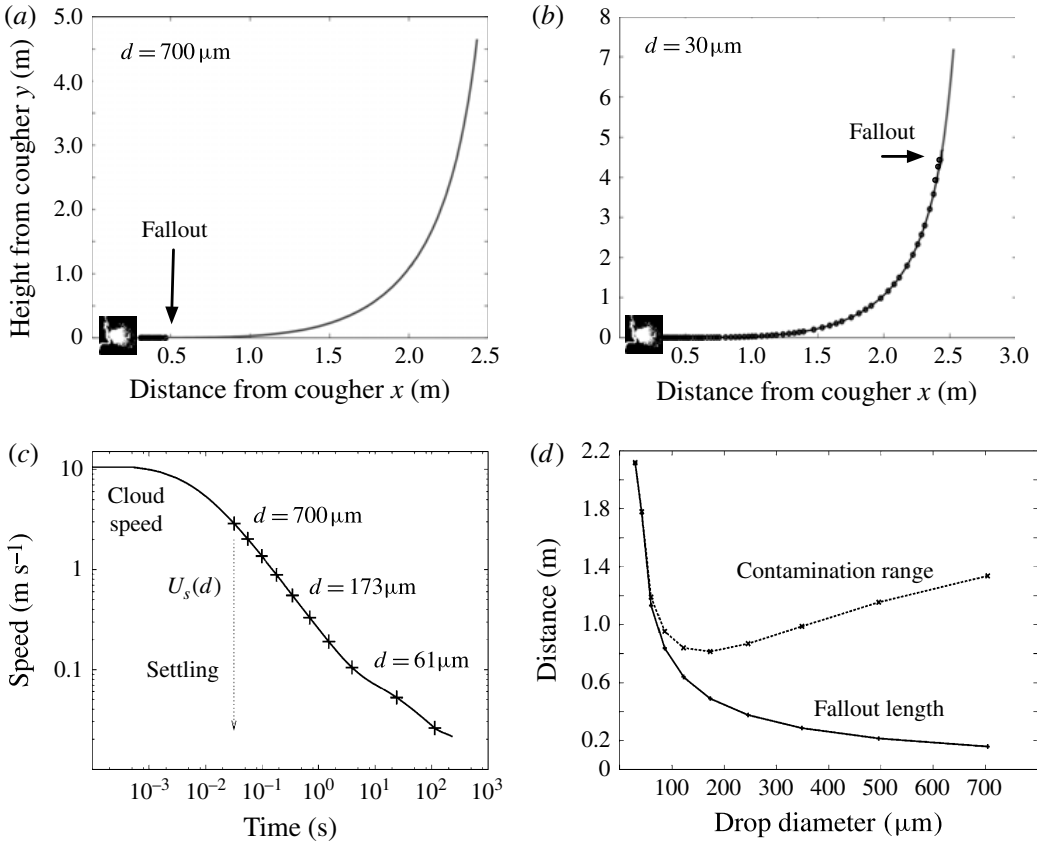

FIGURE 18. Application of our model to realistic cough clouds containing monodisperse droplets. Trajectories of the clouds containing only particles of diameter (*a*) $d = 700$ μm or (*b*) $d = 30$ μm. (*c*) The cloud speed is compared with the settling speed of the droplets of various sizes, thus indicating their fallout time. (*d*) The non-monotonic dependence of the range on drop diameter arises because larger suspended droplets fall out earlier in the life of the cloud, hence with higher exit velocities than smaller drops that fall out later.

fluid in a self-similar manner, leading to the increase of its size and decrease of its mean speed with distance from the source. We have proposed both discrete and continuous fallout models that draw from previous models of multiphase plume (Morton *et al.* 1956; Bush *et al.* 2003) and sedimentation dynamics (Martin & Nokes 1988). In the discrete fallout model, droplets remain suspended until their settling speed exceeds the mean speed of the cloud, at which point they fall out. In the continuous fallout model, droplets leave the bottom part of the cloud continuously at a rate prescribed by the size of the cloud and the settling speed of the droplets. Analogue experiments were used to test the range of validity of our theoretical model. Both the multiphase cloud trajectory and the deposition range of the analogue droplets were compared against experimental results and showed satisfactory match. Thus, we applied the theoretical model to an example of a clinical data set focusing on cough parameters in winter indoor conditions.

Our key findings are as follows. The turbulent multiphase cloud plays a critical role in extending the range of the majority of pathogen-bearing drops that accompany human coughs and sneezes. Smaller droplets (less than 50 μm diameter) can remain suspended in the cloud long enough for the cough to reach heights where ventilation

systems can be contaminated (4–6 m). A droplet of diameter $d = 10$ μm evaporates in 0.027 s, during which it would fall a distance of approximately 0.08 mm at a settling speed of approximately 3 mm s^{-1}. It would thus clearly remain suspended in a cough or sneeze cloud metres away from the cougher. Indeed, the cloud model presented in this study predicts that the range of droplets of diameter $d \leqslant 100$ μm would be extended by a factor of 5 to more than 200 as d decreases from 100 to 10 μm. Moreover, following fallout from the cloud, such small droplets or their associated droplet nuclei can be resuspended by ambient air currents that usually have speeds of the order of $\sim$1 cm s^{-1} (e.g. Melikov & Kaczmarczyk 2012).

The ambient conditions also influence the buoyancy of the cloud and so the range of contamination of its suspended droplets. Changing the buoyancy from summer to winter indoor conditions can result in a variation of the range of deposition of the order of metres for the relatively large droplets (diameter $d > 50$ μm) to dozens of metres for the smallest droplets and droplet nuclei (diameter $d < 10$ μm). We note also that droplet evaporation can enhance the cloud buoyancy, increasing its vertical momentum and thus the chances of the cloud reaching the ceiling and contaminating the ventilation system.

Finally, we note that problems arising in disease transmission are numerous, and constitute a rich class of problems to which the tools of fluid dynamics can be profitably brought to bear. The use of multiphase turbulent flow theory has enabled us to revise the existing physical picture of respiratory disease transmission. Specifically, we have developed a theoretical model that can be used with clinical data to yield improved estimates of the range of airborne respiratory disease transmission. A more thorough integration of our theoretical model with clinical data is the subject of our continuing work.

Acknowledgements

The authors thank Alex Techet at the Experimental and Hydrodynamics Laboratory at MIT for the use of the water tank where the analogue experiments were performed. The authors thank the MIT Edgerton Center for giving access to some of the high-speed cameras used to visualize the flows. The authors gratefully acknowledges the financial support of the National Science Foundation (Grant DMS-1022356) and LB likewise the Natural Sciences and Engineering Research Council of Canada.

Appendix

For relatively large droplets, three regimes of drag are used: the turbulent regime ($Re > 1000$), the transition regime ($0.5 < Re \leqslant 1000$) and the Stokes regime ($Re < 0.5$). For the largest drops in the turbulent regime $Re > 1000$, $U_s^t = 8ag/(3 \times 0.44\rho_a)(\rho_p - \rho_a)$. In the intermediate regime, $U_s^t = \mu/(2a\rho_a)\exp[-3.07 + 0.9935J - 0.0178J^2]$, with $J = \log[4(\rho_p - \rho_a)\rho_a(2a)^3 g/(3\mu^2)]$ (see e.g. Hinds 1999, p. 57). The Stokes settling speed is $U_s^t = 2ga^2/(9\mu)(\rho_p - \rho_a)$.

In standard conditions, the mean free path in air is $\lambda \approx 100$ nm and its ratio with the size of a suspended particle d defines the Knudsen number $K_n = \lambda/d$. Slip becomes important for $0.1 \lesssim K_n$, corresponding to particles with diameters $d < 1$ μm, while it is negligible for particles with $d > 10$ μm (Lauga *et al.* 2005; Crowder *et al.* 2001; Hinds 1999; Kajihara 1971; Cunningham 1910). In between these two sizes, in standard air conditions, additional drag is felt by the droplet due to the breakdown of the no-slip hypothesis and a correction factor to Stokes law needs to be introduced.

REFERENCES

BLANCHETTE, F. A. 2003 Sedimentation in a stratified ambient. PhD thesis, MIT, Cambridge.

BOUROUIBA, L. & BUSH, J. W. M. 2012 Drops and bubbles. In *Handbook of Environmental Fluid Dynamics Volume One: Overview and Fundamentals* Taylor & Francis.

BUSH, J. W. M., THURBER, B. A. & BLANCHETTE, F. 2003 Particle clouds in homogeneous and stratified environments. *J. Fluid Mech.* **489**, 29–54.

CARDOSO, S. S. S. & WOODS, A. W. 1993 Mixing by a turbulent plume in a confined stratified region. *J. Fluid Mech.* **250**, 277–305.

CLARK, R. P. & DE CALCINA-GOFF, M. L. 2009 Some aspects of the airborne transmission of infection. *J. R. Soc. Interface* **6**, S767–S782.

CLARKE, J. C., BUSH, A. B. G. & BUSH, J. W. M. 2009 Freshwater discharge, sediment transport, and modeled climate impacts of the final drainage of glacial lake Agassiz. *J. Climate* **22**, 2161–2180.

CROWDER, T. M., ROSATI, J. A., SCHROETER, J. D., HICKEY, A. J. & MARTONEN, T. B. 2001 Fundamental effects of particle morphology on lung delivery: predictions of Stokes' law and the particular relevance to dry powder inhaler formulation and development. *Pharm. Res.* **19**, 239–245.

CUNNINGHAM, E. 1910 On the velocity of steady fall of spherical particles through fluid medium. *Proc. R. Soc. Lond.* A **83** (563), 357–365.

DUGUID, J. P. 1945 The numbers and the sites of origin of the droplets expelled during expiratory activities. *Edinburgh Med. J.* **LII** (II), 385–401.

DUGUID, J. P. 1946 The size and the duration of air-carriage of respiratory droplets and droplet-nuclei. *J. Hyg.* **44** (6), 471–479.

EDWARDS, D. A., BEN-JEBRIA, A. & LANGER, R. 1998 Recent advances in pulmonary drug delivery using large, porous inhaled particles. *J. Appl. Physiol.* **85**, 379–385.

GHOSH, S., DÁVILA, J., HUNT, J., SRDIC, A., FERNANDO, H. & JONAS, P. 2005 How turbulence enhances coalescence of settling particles with applications to rain in clouds. *Proc. R. Soc. A: Math. Phys. Engng* **461** (2062), 3059–3088.

GONNERMANN, H. M. & MANGA, M. 2007 The fluid mechanics inside a volcano. 321–356.

GUPTA, J. K., LIN, C. H. & CHEN, Q. 2009 Flow dynamics and characterization of a cough. *Indoor Air* **19**, 517–525.

HINDS, W. C. 1999 *Aerosol Technology: Properties, Behavior, and Measurement of Airborne Particles*. John Wiley & Sons, Inc..

HOLTERMAN, H. J. 2003 Kinetics and evaporation of water drops in air. *Tech. Rep.* IMAG Report 2003, Wageningen, Netherlands.

HÖPPE, P. 1981 Temperatures of expired air under varying climatic conditions. *Intl J. Biometeorol.* **25**, 127–132.

HUNT, J. C. R., DELFOS, R., EAMES, I. & PERKINS, R. J. 2007 Vortices, complex flows and inertial particles. *Flow Turbul. Combust.* **79**, 207–234.

HUNT, G. R. & KAYE, N. G. 2001 Virtual origin correction for lazy turbulent plumes. *J. Fluid Mech.* **435**, 377–396.

IMF/WORLD BANK, 2006 Press briefing: Avian flu. In *Proc. IMF/World Bank Annual Meetings* Suntec.

JOHNSON, G., MORAWSKA, L., RISTOVSKI, Z., HARGREAVES, M., MENGERSEN, K., CHAO, C., WAN, M., LI, Y., XIE, X., KATOSHEVSKI, D. & CORBETT, S. 2011 Modality of human expired aerosol size distributions. *J. Aerosol Sci.* **42**, 839–851.

JONASSEN, D. R., SETTLES, G. S. & TRONOSKY, M. D. 2006 Schlieren PIV for turbulent flows. *Opt. Lasers Engng* **44**, 190–207.

KAJIHARA, M. 1971 Settling velocity and porosity of suspended particle. *J. Oceanogr. Soc. Japan* **27**, 158–162.

LAI, A., ZHAO, B., LAW, A. -K. & ADAMS, E. 2013 Two-phase modeling of sediment clouds. *Environ. Fluid Mech.* 1–29.

LAUGA, E., BRENNER, M. P. & STONE, H. A. 2005 Microfluidics: the no-slip boundary condition. *Handbook of Experimental Fluid Dynamics*. Springer.

LEE, W. Y., LI, A. C. Y., LEE, J. H. W. & ASCE, F. 2013 Structure of a horizontal sediment-laden momentum jet. *J. Hydraul. Engng* **139**, 124–140.

LOUDON, R. & ROBERTS, M. 1967 Relation between the airborne diameters of respiratory droplets and the diameter of the stains left after recovery. *Nature* **213**, 95–96.

MARTIN, D. & NOKES, R. 1988 Crystal settling in a vigorously convecting magma chamber. *Nature* **332**, 534–536.

MCCOOL, F. D. 2006 Global physiology and pathophysiology of cough. *Chest* **129** (1 Suppl), 48S–53S.

MCCUTCHAN, J. W. & TAYLOR, C. L. 1981 Respiratory heat exchange with varying temperature and humidity of inspired air. *J. Appl. Physiol.* **4**, 121–135.

MELIKOV, A. K. & KACZMARCZYK, J. 2012 Air movement and perceived air quality. *Build. Environ.* **47**, 400–409.

MORAWSKA, L. 2006 Droplet fate in indoor environments, or can we prevent the spread of infection?. *Indoor Air* **16**, 335–347.

MORAWSKA, L., JOHNSON, G., RISTOVSKI, Z., HARGREAVES, M., MENGERSEN, K., CORBETT, S., CHAO, C., LI, Y. & KATOSHEVSKI, D. 2009*a* Size distribution and sites of origin of droplets expelled from the human respiratory tract during expiratory activities. *Aerosol Sci.* **40**, 256–259.

MORAWSKA, L., JOHNSON, G., RISTOVSKI, Z., HARGREAVES, M., MENGERSEN, K., CORBETT, S., CHAO, C., LI, Y. & KATOSHEVSKI, D. 2009*b* Size distribution and sites of origin of droplets expelled from the human respiratory tract during expiratory activities. *J. Aerosol Sci.* **40**, 256–269.

MORTON, B. R., TAYLOR, G. I. & TURNER, J. S. 1956 Turbulent gravitational convection from maintained and instantaneous sources. *Proc. R. Soc. Lond.* **234**, 1–23.

NICAS, M., NAZAROFF, W. W. & HUBBARD, A. 2005 Toward understanding the risk of secondary airborne infection: emission of respirable pathogens. *J. Occup. Environ. Hyg.* **2**, 143–154.

PAPINENI, R. S. & ROSENTHAL, F. S. 1997 The size distribution of droplets in the exhaled breath of healthy human subjects. *J. Aerosol Med.* **10**, 105–116.

PARK, J., KANG, S., LEE, S. & KIM, W. C. D. 2010 How respiratory muscle strength correlates with cough capacity in patients with respiratory muscle weakness. *Yonsei Med. J.* **51**, 392–397.

PICARD, A., DAVIS, R. S., GLÄSER, M. & FUJII, K. 2008 Revised formula for the density of moist air (CIPM-2007). *Metrologia* **45**, 149–155.

RICHARDS, J. M. 1961 Experiments on the penetration of an interface by buoyant thermals. *J. Fluid Mech.* **11**, 369–384.

RICHARDS, J. M. 1965 Puff motions in unstratified surroundings. *J. Fluid Mech.* **21**, 97–106.

SCORER, R. S. 1957 Experiments on convection of isolated masses of buoyant fluid. *J. Fluid Mech.* **2**, 583–594.

SCORER, R. S. 1978 *Environmental Aerodynamics*. Ellis Horwood.

SETTLES, G. S. 2006 Fluid mechanics and homeland security. *Annu. Rev. Fluid Mech.* **38**, 87–110.

SOCOLOFSKY, S. A., CROUNSE, B. C. & ADAMS, E. E. Environmental fluid mechanics: theories and applications. In *Multi-Phase Plumes in Uniform, Stratified, and Flowing Environments* American Society of Civil Engineers.

SONKIN, L. S. 1951 The role of particle size in experimental airborne infection. *Am. J. Hyg.* **53**, 337–354.

TANG, J. W., LI, Y., EAMES, I., CHAN, P. & RIDGWAY, G. 2006 Factors involved in the aerosol transmission of infection and control of ventilation in healthcare premises. *J. Hosp. Infect.* **64**, 100–114.

TANG, J. W., LIEBNER, T. J., CRAVEN, B. A. & SETTLES, G. S. 2009 A schlieren optical study of the human cough with and without wearing masks for aerosol infection control. *J. R. Soc. Interface* **6**, S727–S736.

TANG, J. W., PATH, F. R. C. & SETTLES, G. S. 2008 Coughing and aerosols. *New Engl. J. Med.* **359**, e19.

TELLIER, R. 2006 Review of aerosol transmission of influenza A virus. *Emerg. Infect. Dis.* **12**, 1657–1662.

TELLIER, R. 2009 Aerosol transmission of influenza A virus: a review of new studies. *J. R. Soc. Interface* **6**, S783–S790.

TURNER, J. S. 1979 *Buoyancy Effects in Fluids*. Cambridge University Press.

WEBER, T. P. & STILIANAKIS, N. I. 2008 Inactivation of influenza A virus in the environment and modes of transmission: a critical review. *J. Infect.* **57**, 361–373.

WELLS, W. F. 1934 On air-born infection. Study II. Droplet and droplet nuclei. *Am. J. Hyg.* **20**, 611–618.

WELLS, W. F. 1955 *Airborne Contagion and Air Hygiene: An Ecological Study of Droplet Infection*. Harvard University Press.

WONG, T. W., LEE, C. K., TAM, W., LAU, J. T., YU, T. S., LUI, S. F., CHAN, P. K., LI, Y., BRESEE, J. S., SUNG, J. J. & PARASHAR, U. D. 2004 Cluster of SARS among medical students exposed to single patient—Hong Kong. *Emerg. Infect. Dis.* **10**, 269–276.

WOODS, A. W. 2010 Turbulent plumes in nature. *Annu. Rev. Fluid Mech.* **42**, 391–412.

YANG, S., LEE, G. W. M., CHEN, C. -M., WU, C. -C. & YU, K. -P. 2007 The size and concentration of droplets generated by coughing in human subjects. *J. Aerosol Med.* **20**, 484–494.

YU, I. T., LI, Y., WONG, T. W., TAM, W., CHAN, A. T., LEE, J. H., LEUNG, D. Y. & HO, T. 2004 Evidence of airborne transmission of the severe acute respiratory syndrome virus. *New Engl. J. Med.* **350**, 1731–1739.

ZAYAS, G., CHIANG, M., WONG, E., MACDONALD, F., LANGE, C., SENTHILSELVAN, A. & KING, M. 2012 Cough aerosol in healthy participants: fundamental knowledge to optimize droplet-spread infectious respiratory disease management. *BMC Pulmonary Med.* **12** (1), 11 doi:10.1186/1471-2466-12-11.